J. Fluid Mech. (2008), *vol.* 606, *pp.* 295–324.
doi:10.1017/S0022112008001730 Printed in the United Kingdom

The self-similar rise of a buoyant thermal in very viscous flow

ROBERT J. WHITTAKER† AND JOHN R. LISTER

Institute of Theoretical Geophysics, Department of Applied Mathematics and Theoretical Physics, University of Cambridge, Wilberforce Road, Cambridge, CB3 0WA, UK

(Received 4 May 2007 and in revised form 20 March 2008)

An exact similarity solution is obtained for the rise of a buoyant thermal in Stokes flow, in which both the rise height and the diffusive growth scale like $t^{1/2}$ as time t increases. The dimensionless problem depends on a single parameter $Ra = B/(\nu\kappa)$ – a Rayleigh number – based on the (conserved) total buoyancy B of the thermal, and the kinematic viscosity ν and thermal diffusivity κ of the fluid. Numerical solutions are found for a range of Ra. For small Ra there are only slight deformations to a spherically symmetric Gaussian temperature distribution. For large Ra, the temperature distribution becomes elongated vertically, with a long wake containing most of the buoyancy left behind the head. Passive tracers, however, are advected into a toroidal structure in the head. A simple asymptotic model for the large-Ra behaviour is obtained using slender-body theory. The width of the thermal is found to increase like $(\kappa t)^{1/2}$, while the wake length and rise height both increase like $(Ra \ln Ra)^{1/2}(\kappa t)^{1/2}$, consistent with the numerical results. Previous experiments suggest that there is a significant transient regime.

1. Introduction

A thermal is an isolated patch of buoyant fluid rising under the influence of gravity. Thermals arise from a finite release of buoyancy, as distinct from plumes which are associated with continuous release. In each case, the source of the buoyancy is usually considered to be temperature, but could be any field that affects the fluid density, such as composition.

Plumes and thermals can either be turbulent, in which case the growth is dominated by turbulent entrainment of ambient fluid (see Morton, Taylor & Turner 1956), or laminar, in which case the growth can be either by straightforward diffusion of the buoyancy field (e.g. Morton 1960) or by laminar entrainment at the rear of a leading vortical head (e.g. Griffiths 1991; Kumagai 2002). Interest in turbulent plumes in the atmosphere grew during the Second World War, and a review of early work is provided by Turner (1969). Such convection has important environmental applications, for example to the atmosphere, oceans and lakes, where viscosities are low and $Pr < 10$. This paper is concerned with very viscous laminar thermals, motivated in part by geophysical applications to convection in the Earth's mantle where the enormous viscosity leads to effectively infinite-Prandtl-number dynamics (typical estimates have $Pr > 10^{20}$).

† Present address: OCIAM, Mathematical Institute, University of Oxford, 24–29 St. Giles, Oxford, OX1 3LB.

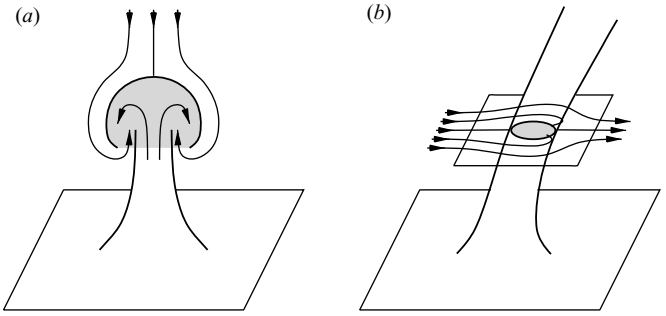

FIGURE 1. Sketches showing the similarity of an isolated thermal to (*a*) the head of a starting plume, and (*b*) the horizontal cross-section of a plume being deflected by a background shear flow.

As well as being an interesting topic in its own right, the study of isolated very viscous thermals may also provide useful insight into the behaviour of the heads of starting plumes and of the cross-sections of steady plumes rising through a sheared background flow. The qualitative relationship between thermals and such plumes is illustrated in figure 1. In experiments (see Griffiths 1991, for example), the vortex-like nature of the head of a starting plume closely resembles that of an isolated thermal (figure 1*a*), though the lower region will be different and the buoyancy content of the head will increase over time owing to continual feed from the plume tail. In a plume that is deflected by a background shear flow (see Griffiths & Campbell 1991, for example), each horizontal cross-section comprises a buoyant region with an ambient flow passing by. This might be expected to yield a similar, albeit two-dimensional, structure to that of an isolated thermal (figure 1*b*).

Very viscous plumes and thermals play a key role in the convection within the Earth's mantle. Surveys of this geophysical background can be found in Steinberger & O'Connell (1998), Nataf (2000), Jellinek & Manga (2004), Hamblin & Christiansen (1998) or Davies (1999), and the references therein. The applications to the Earth's mantle have prompted many experimental, theoretical and numerical studies of viscous starting plumes (e.g. Olson & Singer 1985; Campbell & Griffiths 1990; Griffiths & Campbell 1990; Moses, Zocchi & Libchaber 1993; Kumagai 2002; Kaminski & Jaupart 2003), steady viscous plumes (e.g. Loper & Stacey 1983; Olson, Schubert & Anderson 1993; Kerr & Mériaux 2004; Whittaker & Lister 2006*a*,*b*), and viscous thermals (e.g. Whitehead & Luther 1975; Griffiths 1986*a*, 1991). Many of these studies have explored the effects of the viscosity ratio between hot and cold material, of laminar entrainment into plumes and the consequent geochemical signatures, and of the interaction of a plume head with an overlying lithospheric lid. Recent investigations (e.g. Jellinek & Manga 2002; Davaille, Girard & Le Bars 2002), have considered coupling between the location of long-lived thermal plumes, such as the Hawaiian hot-spot, and the topography on a compositionally dense layer at the base of the mantle, which may itself have large radiogenic heating (Boyet & Carlson 2005; Tolstikhin & Hofmann 2005; Buffett 2002).

In this paper we put many of these complications – boundaries, variable viscosity, compositional effects – aside for the moment, and re-examine one of the fundamental problems in convection, namely the rise and growth of an isolated very viscous thermal. Further discussion of generalizations and applications is deferred to § 6. Two previous papers are of particular relevance to the theoretical solutions we derive here.

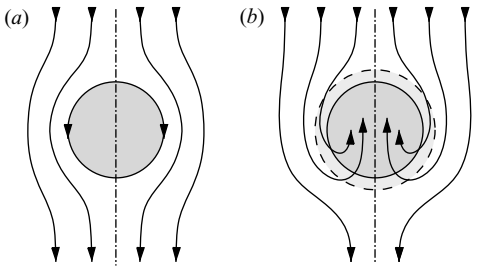

FIGURE 2. Sketches of the flow envisaged in the large-Rayleigh-number model of Griffiths (1986*a*). (*a*) Instantaneous velocity in a frame moving upwards with the centre of buoyancy. (*b*) Material pathlines in a frame moving and expanding with the thermal.

First, Morton (1960) examined the case of a weak thermal (Rayleigh number $Ra \ll 1$) at $O(1)$ Prandtl number, and calculated the leading-order solution for $Pr = 1$. In this regime, the flow produces only a small perturbation to the spherically symmetric diffusing Gaussian solution. In this paper, we describe a significant generalization of the work of Morton (1960) to fully non-linear thermals ($Ra \geqslant O(1)$) in Stokes flow (i.e. at infinite Prandtl number). Advection is at least as important as diffusion and the temperature field is greatly distorted from symmetry about the origin.

Secondly, Griffiths (1986*a*) developed a large-Rayleigh-number model for an isolated viscous thermal. Based on experimental observations, it was assumed that such a thermal comprises a reasonably well-mixed spherical core, surrounded by an expanding thermal boundary layer that is completely entrained into the core at the rear of the thermal (see figure 2). Equations were derived linking the thermal's radius, growth rate, buoyancy and rise velocity, and these were then solved to determine the behaviour explicitly as a function of time and Rayleigh number (to within a set of $O(1)$ multiplicative pre-factors). The width of the thermal boundary layer was estimated by a diffusive growth of $(\kappa t_a)^{1/2}$ over an advection time t_a given by the thermal's radius and rise velocity, where κ is the thermal diffusivity. The mass flux into the boundary layer determined the rate of overall growth in volume of the thermal, and the rise velocity was assumed (up to an $O(1)$ scaling factor) to be that of a spherical drop in Stokes flow.

Two questions naturally arise regarding the assumptions of this model: how well-mixed and spherical is the core region, and is the thermal boundary layer completely entrained without any buoyancy being left behind the core as a tail or wake? As we shall see, our calculations show that a significant thermal wake containing most of the buoyancy is eventually left behind the head, and that the head is not particularly well-mixed.

There is a loose link here with work on the rise of a compositionally buoyant viscous drop for which diffusion is negligible (e.g. Kojima, Hinch & Acrivos 1984; Koh & Leal 1989; Pozrikidis 1990; Garcimartin, Mancini & Perezgarcia 1992). In the absence of surface tension, such a drop is found to be unstable, with a thin filament-like tail left behind the rear of an initially almost spherical head. A similar tail is shed behind a nearly spherical cloud of sedimenting particles at low Reynolds number (e.g. Machu *et al.* 2001, Metzger, Nicolas & Guazzelli 2007). In both situations the leading patch of buoyant material can subsequently evolve into a torus, which then becomes unstable. It should be noted, however, that diffusion is usually considered negligible (on the relevant time scale) for compositional drops and that the 'diffusion' of a cloud of particles occurs through complex hydrodynamic interactions between the particles.

Neither situation is thus fully analogous to a thermal, for which we show that the long-time structure is governed by a balance between diffusion and advection even at large Rayleigh number.

This paper is organized as follows. In § 2, we formalize the problem of an isolated thermal in Stokes flow, and show that the diffusive growth and height of rise of the thermal have the same temporal scaling ($t^{1/2}$). We are thus able to find an exact similarity solution. With suitable scalings (see § 2.2), the similarity equations depend only on a single dimensionless parameter

$$Ra = \frac{B}{\nu\kappa}, \tag{1.1}$$

where B is the total buoyancy of the thermal (defined formally in (2.5)), and ν and κ are respectively the kinematic viscosity and thermal diffusivity of the fluid. Numerical solutions for varying values of Ra are described in § 3 and § 4. As $Ra(\rightarrow 0$, the heat and Stokes equations decouple, there is no advection of heat, and we obtain Morton's leading-order Gaussian temperature distribution centred on the origin. For a weak thermal ($Ra = O(100)$), we obtain a slight deformation of the Gaussian solution, vertically translated by the mean rise velocity, and with diffusive effects (favouring a return to spherical symmetry) balancing weak advective effects (which deform the temperature contours slightly). For larger Ra, we obtain significant deformation of the temperature distribution away from spherical symmetry, and at large Ra the distribution is vertically elongated and carrot-shaped. A simple asymptotic model based on application of slender-body theory to this structure is proposed for the behaviour at large Ra in § 5 and tested against the full numerical solutions. Concluding remarks, including a detailed comparison with the model of Griffiths (1986*a*), can be found in § 6.

2. Problem description and formulation

2.1. *Governing equations*

We consider the rise of an isolated thermal whose buoyancy is solely attributable to a temperature $T(\boldsymbol{x}, t)$ that exceeds the uniform background temperature T_0. We use the Boussinesq approximation, and assume that the viscosity ν, thermal diffusivity κ and thermal expansivity β are all constant. Inertia, viscous heating and non-Newtonian effects are assumed to be negligible. The governing equations are therefore

$$\nu\nabla^2\boldsymbol{u} = \frac{1}{\rho_0}\nabla p + g[1-\beta(T-T_0)]\hat{\boldsymbol{e}}_z, \tag{2.1}$$

$$\nabla\cdot\boldsymbol{u} = 0, \tag{2.2}$$

$$\frac{\partial T}{\partial t} + (\boldsymbol{u}\cdot\nabla)T = \kappa\nabla^2 T, \tag{2.3}$$

where $\boldsymbol{u}$ is the fluid velocity and p the pressure. The ambient fluid density is ρ_0 and the acceleration due to gravity is $-g\hat{\boldsymbol{e}}_z$, where $\hat{\boldsymbol{e}}_z$ is the unit vertical vector. We work in an unbounded domain, with the far-field conditions

$$\boldsymbol{u}\rightarrow\boldsymbol{0}, \quad p+\rho_0 gz\rightarrow p_0 \quad \text{and} \quad T\rightarrow T_0 \quad \text{as} \quad |\boldsymbol{x}|\rightarrow\infty. \tag{2.4}$$

We define the total buoyancy

$$B = g\beta\int (T-T_0)\,\mathrm{d}^3x, \tag{2.5}$$

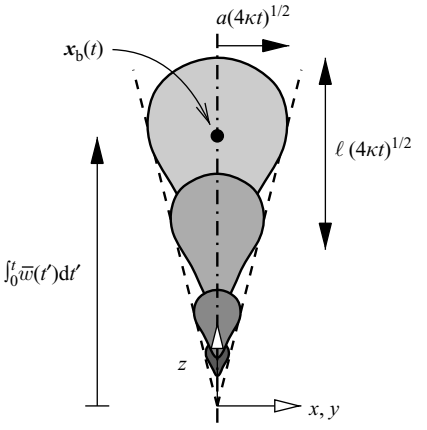

FIGURE 3. A sketch of the rising thermal. Diffusion of heat causes the extent of the thermal to increase like $t^{1/2}$, and the temperature difference to decay like $t^{-3/2}$. Since the mean rise velocity $\overline{w} \propto t^{-1/2}$, the rise height also scales like $t^{1/2}$ and so the region swept out by the thermal is a cone. The dependence of the dimensionless radial and vertical scales a and ℓ on the Rayleigh number Ra is described in § 5.

which is conserved by virtue of (2.2)–(2.4) and is assumed to be finite. We define the centre of buoyancy $\boldsymbol{x}_b$ in the natural way by

$$\boldsymbol{x}_b(t) = \frac{g\beta}{B} \int \boldsymbol{x}\,(T - T_0)\,\mathrm{d}^3x, \tag{2.6}$$

and choose the coordinate origin so that $\boldsymbol{x}_b(0) = \boldsymbol{0}$. Finally, we define a mean rise velocity $\overline{w}$ by the buoyancy-weighted average

$$\overline{w}(t) = \frac{g\beta}{B} \int (\hat{\boldsymbol{e}}_z \cdot \boldsymbol{u})(T - T_0)\,\mathrm{d}^3x. \tag{2.7}$$

By differentiating (2.6) with respect to time, substituting from (2.3) and (2.2), and integrating by parts, we deduce that

$$\hat{\boldsymbol{e}}_z \cdot \frac{\mathrm{d}\boldsymbol{x}_b}{\mathrm{d}t} = \overline{w}. \tag{2.8}$$

Therefore $\overline{w}$ is also the speed at which the centre of buoyancy rises through the fluid, and

$$z_b(t) = \int_0^t \overline{w}(t')\,\mathrm{d}t'. \tag{2.9}$$

For simplicity, we shall restrict our attention to axisymmetric thermals. The apparent ease of producing axisymmetric thermals in experiments (e.g. Whitehead & Luther 1975; Griffiths 1986*b*) suggests that an axisymmetric configuration is stable to sufficiently small perturbations, most probably through the smoothing action of diffusion.

A sketch of the situation under consideration is shown in figure 3.

2.2. *Similarity representation*

With a purely diffusive solution, the length scale L of the thermal would increase like $(\kappa t)^{1/2}$, and hence the temperature difference $T - T_0$ would decay in proportion to $t^{-3/2}$ in order to satisfy buoyancy conservation. The velocity in the Stokes flow

induced by a total buoyancy B distributed over a length scale L is readily shown (cf. the rise velocity of a sphere) to scale like $B/\nu L \propto Ra(\kappa/t)^{1/2}$. The distance risen will thus scale like $\int t^{-1/2}\,\mathrm{d}t \propto t^{1/2}$, which is the same as the distance spread by diffusion (see figure 3). It is therefore possible to seek a similarity solution in which all lengths are scaled with $(4\kappa t)^{1/2}$.

We introduce a similarity position vector $\boldsymbol{\xi}$ defined by

$$\boldsymbol{\xi} = \frac{\boldsymbol{x}}{(4\kappa t)^{1/2}}. \tag{2.10}$$

The dependent variables are then represented in the similarity solution as follows:

$$T(\boldsymbol{x}, t) - T_0 = \frac{B}{g\beta(4\kappa t)^{3/2}}\,\Theta(\boldsymbol{\xi}), \tag{2.11}$$

$$\boldsymbol{u}(\boldsymbol{x}, t) = \frac{\kappa}{(4\kappa t)^{1/2}}\,\boldsymbol{U}(\boldsymbol{\xi}), \tag{2.12}$$

$$p(\boldsymbol{x}, t) - p_0 + \rho_0 g z = \frac{\rho_0 \nu}{4t} P(\boldsymbol{\xi}). \tag{2.13}$$

We shall make use of both cylindrical polar coordinates (ρ, ϕ, ζ) with corresponding unit vectors $(\hat{\boldsymbol{e}}_\rho, \hat{\boldsymbol{e}}_\phi, \hat{\boldsymbol{e}}_\zeta)$, and spherical polar coordinates (ξ, θ, ϕ). The axial vector $\hat{\boldsymbol{e}}_\zeta$ and spherical axis $\theta = 0$ are defined to point vertically upwards.

For the numerical method described in § 4.1, we retain a time-dependence in the system, in order to use the temporal convergence towards the similarity solution. If we allow Θ to depend on t as well as $\boldsymbol{\xi}$, and substitute (2.10)–(2.13) into (2.3), then the resultant appearance of the group $4t(\partial/\partial t)$ shows that the natural time-like variable in similarity space is $\tau = \frac{1}{4}\ln t$.

Under the change of variables from $(\boldsymbol{x}, t)$ to $(\boldsymbol{\xi}, \tau)$, the governing equations (2.1)–(2.3) become

$$\nabla^2 \boldsymbol{U} = \nabla P - Ra\,\Theta \hat{\boldsymbol{e}}_\zeta, \tag{2.14}$$

$$\nabla \cdot \boldsymbol{U} = 0, \tag{2.15}$$

$$\frac{\partial \Theta}{\partial \tau} + \nabla \cdot \Big((\boldsymbol{U} - 2\boldsymbol{\xi})\,\Theta \Big) = \nabla^2 \Theta, \tag{2.16}$$

where the gradients are now with respect to $\boldsymbol{\xi}$. The addition of $-2\boldsymbol{\xi}$ to the velocity $\boldsymbol{U}$ in (2.16) arises from the coordinate transformation (2.10), and reflects the fact that a point at fixed physical position $\boldsymbol{x}$ moves towards the origin of the expanding coordinate system $\boldsymbol{\xi}$. The desired similarity solution is a steady (τ-independent) solution for $\boldsymbol{U}$, P and Θ, and the τ-dependence in (2.16) describes the evolution towards such a steady state.

The boundary conditions (2.4) and buoyancy normalization (2.5) become

$$\boldsymbol{U} \to \boldsymbol{0}, \quad P \to 0 \quad \text{and} \quad \Theta \to 0 \quad \text{as} \quad |\boldsymbol{\xi}| \to \infty, \tag{2.17}$$

$$\int \Theta \,\mathrm{d}^3\xi = 1. \tag{2.18}$$

Finally, the similarity form of the mean rise velocity is given by

$$\overline{w}(t) = \frac{\kappa}{(4\kappa t)^{1/2}}\,\overline{W}, \quad \text{where} \quad \overline{W} = \int (\hat{\boldsymbol{e}}_\zeta \cdot \boldsymbol{U})\,\Theta \,\mathrm{d}^3\xi. \tag{2.19}$$

We shall calculate the steady solutions of (2.14)–(2.18), which now depend only upon the single dimensionless parameter Ra. This parameter is a Rayleigh number

(since it gives the strength of the forcing), but it can also be thought of as a Péclet number (since it determines the relative strength of advection in the heat equation). It is the same as the parameter A of Morton (1960).

2.3. *Neglect of inertia*

In § 2.1, we assumed that inertia was negligible. The Reynolds number of the flow is

$$Re = \max\{\overline{W}\ell\kappa/\nu, \kappa/\nu\}, \tag{2.20}$$

where ℓ is an appropriate dimensionless length scale in the similarity frame. The two possibilities in (2.20) arise from considering the neglected nonlinear and unsteady terms, respectively, in the Navier–Stokes equations. Owing to the form of the similarity solution, the Reynolds number (2.20) has no explicit time dependence. Substituting the scalings (5.14) and (5.17) for ℓ and $\overline{W}$ (from the analysis of § 5.1) into (2.20) and requiring $Re \ll 1$, we find that the Prandtl number $Pr = \nu/\kappa$ must satisfy

$$Pr \gg \max\{Ra \ln Ra, 1\} \tag{2.21}$$

for inertia to be negligible. This condition is easily satisfied within the Earth's mantle, for example.

3. Series expansion for small Rayleigh number

To solve the similarity system (2.14)–(2.18), we first briefly consider a formal series expansion for $Ra \ll 1$. Each of the variables is expanded in powers of Ra (e.g. $\Theta = \Theta^{(0)} + Ra\,\Theta^{(1)} + Ra^2\,\Theta^{(2)} + \cdots$). The use of spherical polar coordinates is found to be convenient.

If we know $\Theta^{(k-1)}$ for some integer k, then we can solve the Stokes equations (2.14) and (2.15) at $O(Ra^k)$ to determine $\boldsymbol{U}^{(k)}$. We can then compute the rise velocity $\overline{W}^{(k)}$ using (2.19), and the $O(Ra^k)$ component of the $\nabla\cdot(\boldsymbol{U}\Theta)$ term in the heat equation (2.16). (Note that $\boldsymbol{U}^{(0)} = \boldsymbol{0}$, so $\Theta^{(k)}$ is not needed.) Finally, we solve the heat equation (2.16) at $O(Ra^k)$ to determine $\Theta^{(k)}$. The process can then be repeated at the next order. This is essentially the same method as that used by Morton (1960) to $O(Ra)$ for a fluid of finite Prandtl number.

3.1. *Analytical progress*

Since $\boldsymbol{U}^{(0)} = \boldsymbol{0}$, the nonlinear advection term is zero at leading order. At $O(1)$, the solution of (2.16) subject to (2.18) is

$$\Theta^{(0)} = \pi^{-3/2}\,\mathrm{e}^{-\xi^2}. \tag{3.1}$$

As expected, the leading-order temperature distribution is a spherically symmetric Gaussian. With this result, (2.14) and (2.15) can be solved at $O(Ra)$ in a number of ways to obtain $\boldsymbol{U}^{(1)}$ and $P^{(1)}$. For example, one can use the well-known solution for an isoviscous spherical drop (see § 4.9 of Batchelor 1967), and integrate over a weighted continuum of these solutions all centred on the origin but with different radii. Alternatively, the Green's function method described in § 3.2 can be employed. Either way, we obtain

$$\begin{aligned}\boldsymbol{U}^{(1)} = {} & \frac{1}{8\pi}\left[\left(\frac{2}{\xi} - \frac{1}{\xi^3}\right)\operatorname{erf}\xi + \frac{2}{\sqrt{\pi}\,\xi^2}\mathrm{e}^{-\xi^2}\right]\cos\theta\,\hat{\boldsymbol{e}}_\xi \\ & + \frac{1}{8\pi}\left[-\left(\frac{1}{\xi} + \frac{1}{2\xi^3}\right)\operatorname{erf}\xi + \frac{1}{\sqrt{\pi}\,\xi^2}\mathrm{e}^{-\xi^2}\right]\sin\theta\,\hat{\boldsymbol{e}}_\theta,\end{aligned} \tag{3.2}$$

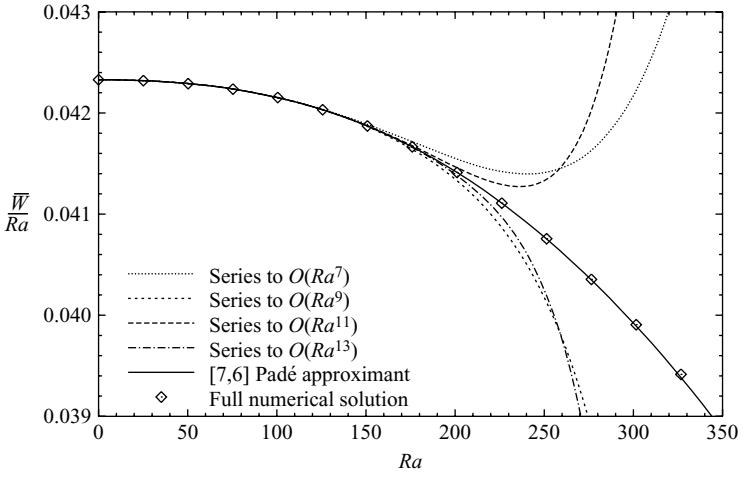

FIGURE 4. The dimensionless rise velocity $\overline{W}$ for small Rayleigh number Ra. Results are computed using the series expansion of § 3 and full numerical method of of § 4. The [7, 6] Padé approximant to the series has singularities at $Ra \approx \pm 259\imath$, consistent with the radius of convergence suggested by the plotted partial sums, and also the pattern of signs in the series.

$$P^{(1)} = \frac{1}{4\pi}\left[\frac{1}{\xi^2}\operatorname{erf}\xi - \frac{2}{\sqrt{\pi}\xi}\mathrm{e}^{-\xi^2}\right]\cos\theta. \tag{3.3}$$

From (2.19) and (3.2), the corresponding leading-order rise velocity is found to be

$$\overline{W}^{(1)} = \frac{1}{3\sqrt{2}\pi^{3/2}} \approx 0.04233. \tag{3.4}$$

In principle, we could now obtain the first correction to the temperature distribution by solving (2.16) at $O(Ra)$. While the solution can be expressed in closed form as a set of integrals, we are unable to evaluate them analytically. However, we do know by symmetry that there is no correction to $\overline{W}$ at the next order. Thus

$$\overline{W} = \frac{Ra}{3\sqrt{2}\pi^{3/2}} + O(Ra^3) \tag{3.5}$$

3.2. *Numerical series expansion*

The series expansion of the previous section has been continued numerically. At $O(Ra^k)$, the solution is a sum over spherical harmonics of degree $n \leqslant k$ multiplied by radial functions that are related by ordinary differential equations. These were solved on a radial grid using a tridiagonal finite-difference scheme to compute the thermal distribution from the advective forcing at each order, and a Green's-function method to compute the Stokes flow from the thermal distribution. Full details can be found in Whittaker (2007).

Terms were computed up to $O(Ra^{40})$. As can be seen in figure 4 the series only converges for $Ra \lesssim 260$. The singularities responsible for the divergence appear to lie on the imaginary-Ra axis, and Padé approximants allow the solution to be extended further on the real axis. This provided a useful check on the accuracy of the full numerical solutions described in § 4, which are able to extend the solution to much larger values of Ra.

4. Numerical solution for larger Rayleigh number

We tried two different numerical approaches to iterate the time-dependent system to steady state at large Ra. The first, based on a spherical-harmonic representation, was limited by numerical stability to $Ra \lesssim 3000$. The second, based on a Green's-function representation on a cylindrical grid, was used successfully to obtain solutions up to $Ra = 10\,000$. Only the second more successful method is described here, but details of the first method can be found in Whittaker (2007).

The first method did however provide the motivation for the second approach. The results showed that the self-similar buoyancy distribution becomes vertically elongated as Ra increases (see figures 6 and 7 below). This makes the spherical-harmonic representation less appropriate, and is probably responsible for the stability issues that limited the method's success.

4.1. *Solution on a cylindrical grid*

Motivated by the apparent solution structure at large Ra, we solved (2.14)–(2.18) on a cylindrical grid. A finite cylindrical domain

$$\mathscr{D} = \{(\rho, \phi, \zeta) : \rho < \rho_{\max},\ \zeta_{\min} < \zeta < \zeta_{\max}\} \tag{4.1}$$

was divided into annular cells

$$\mathscr{D}_{ij} = \{(\rho, \phi, \zeta) : \rho_{i-1} < \rho < \rho_i,\ \zeta_{j-1} < \zeta < \zeta_j\}, \tag{4.2}$$

with the $N+1$ points $\{\rho_i\}$ and $M+1$ points $\{\zeta_j\}$ being uniformly spaced. The temperature was represented by the value at the centre of each cell, and the velocity by the normal components across each of the cell boundaries. The domain size was chosen to be sufficiently large that the steady-state temperature at the domain boundaries was typically less than 10^{-10} times the peak value.

Using the time-dependent heat equation (2.16), we iterated towards a steady state by alternately solving the Stokes equations (with the previous buoyancy distribution) and the heat equation (with the previous velocity field). We used a Green's-function representation (see Appendix A) for the Stokes equations, and a finite-difference 'Alternating Direction Implicit' (ADI) scheme (see Press *et al.* 1986, § 17.6) for the heat equation. The ADI scheme was written to conserve heat at each time step, and we applied a no-heat-flux boundary condition on the (artificial) external boundaries of the domain.

The time-consuming part of each time step is the computation of the velocity using the Green's function, which is an $O(N^2M^2)$ process. To improve efficiency, we performed several ADI steps on the heat equation before re-computing the velocity field, and also neglected velocity contributions from outer points where the temperature is less than a small threshold value (typically 10^{-8}). In addition, the velocity field (which is significantly smoother than the temperature field) was computed directly from the Green's function at only a quarter of the grid-points. Interpolation was then used to fill in the gaps.

For larger values of Ra, a small time step was required for stability, and the steady state was approached by exponentially modulated sinusoidal oscillations. The period of oscillation was independent of the time step used, and could be several thousands of time steps long. The perturbations in the buoyancy distribution were concentrated in the head region, and the period of the oscillations was comparable with the circulation period of the relative effective advection velocity around the vortex in the head (see figures 7 and 12 below). We therefore attribute the oscillations to a physical eigenmode of the system rather than a numerical artifact, probably involving

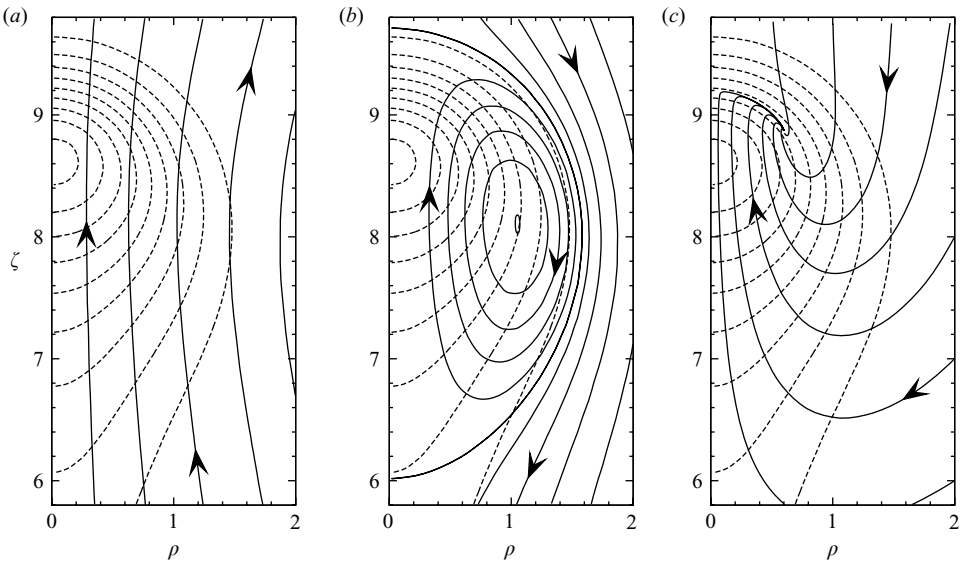

FIGURE 5. Plots of various velocity fields (solid) and temperature contours (dashed) at $Ra = 400$. (*a*) Streamlines of the similarity velocity $\boldsymbol{U}$. (*b*) Streamlines of the velocity $\boldsymbol{U} - \overline{W}\hat{\boldsymbol{e}}_\zeta$ relative to the rising centre of buoyancy at $\zeta_b = 7.58$. (*c*) Material pathlines corresponding to the effective advection velocity $\boldsymbol{U} - 2\boldsymbol{\xi}$ in the expanding similarity frame. Owing to the $t^{1/2}$ growth of the thermal, plot (*c*) gives a more useful representation of the flow than either of the instantaneous streamline plots.

the advection of an initial thermal anomaly around the head while it decays slowly towards the similarity solution.

To speed up the convergence (since we are principally interested in finding the steady state), it was convenient occasionally to stop the time stepping and to average the temperature distributions from two antipodal times of the oscillation. The time stepping was then restarted from this new distribution and the process could be repeated. For larger Ra this was found to be very effective at accelerating the convergence to steady state.

4.2. *Results*

Figures 6–8 and 12 show how the computed similarity velocity and temperature fields change as Ra increases, while figures 9–11 show different aspects of the solution for $Ra = 3000$. The streamlines of $\boldsymbol{U}$, the velocity relative to the origin, are not a very instructive way to visualize the velocity field, since the vertical component of $\boldsymbol{U}$ is everywhere positive (e.g. figure 5*a*). A better alternative is to consider the velocity relative to another reference point fixed in the expanding similarity frame. For example, $\boldsymbol{U} - \overline{W}\hat{\boldsymbol{e}}_\zeta$ describes flow relative to the rising centre of buoyancy (e.g. figure 5*b*). However, whichever reference point is chosen, the resulting streamlines lose significance away from that point, owing to the time-dependence of the diffusing flow. This is especially important for larger Ra when the buoyancy distribution is highly elongated, so that even the centre of buoyancy is not a good reference point for the whole flow. Instead, we visualize the flow using the trajectories of material fluid elements in the similarity frame (e.g. figure 5*c*). These are given by the vector field $\boldsymbol{U} - 2\boldsymbol{\xi}$, which is also the effective advection velocity in the heat equation (2.16). The pathlines defined by this 'velocity' field indicate how both fluid elements and

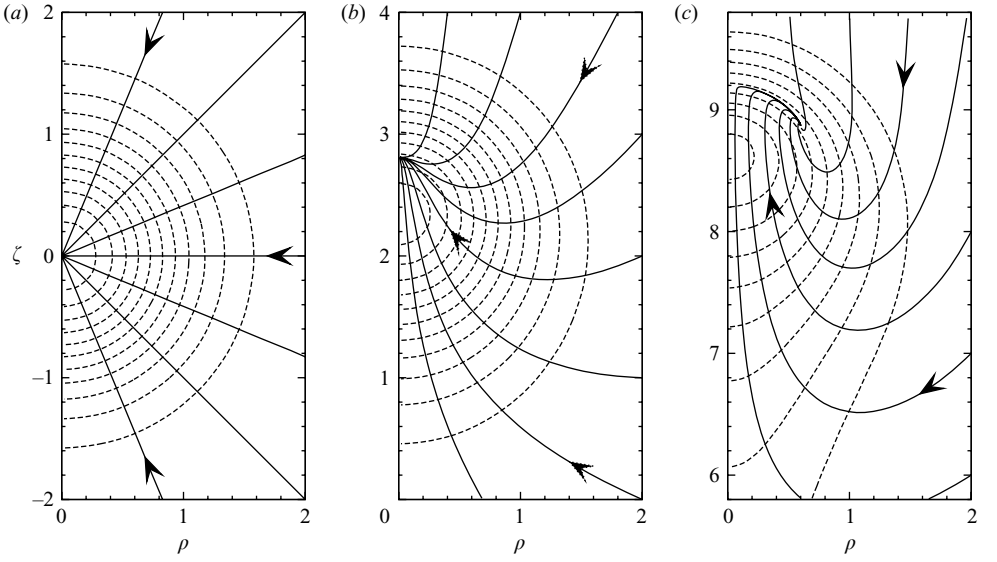

FIGURE 6. Plots of the velocity (solid) and temperature contours (dashed) for (*a*) $Ra = 0$, (*b*) $Ra = 100$ and (*c*) $Ra = 400$. The solid lines are pathlines corresponding to the effective advection velocity $\boldsymbol{U} - 2\boldsymbol{\xi}$, which show material trajectories in the expanding similarity frame. As Ra increases, the temperature distribution is displaced vertically. It is still roughly spherical at $Ra = 100$, but by $Ra = 400$ a noticeable wake is left behind the main head, which extends back to $\zeta = 0$.

heat are transported, and provide a good intuitive feel for the flow in the expanding similarity frame.

For small Ra (see figure 6*a*), the buoyancy distribution is roughly spherical and the material pathlines converge on a nodal point on the axis. As Ra increases, the buoyancy distribution starts to elongate vertically with a 'tail' forming below the 'head'.

At $Ra \approx 100$ (figure 6*b*), the node moves away from the axis, forming an attracting ring and leaving a saddle point behind (figure 6*c*). This transition occurs when the outward radial velocity U_ρ generated by the buoyancy becomes greater than the inward radial advection -2ρ due to the coordinate transformation. For larger Ra the pathlines approach the attracting ring in a spiral manner.

For $Ra \gtrsim 300$, the buoyancy distribution shows a clear wake or tail protruding behind a more spherical head region (figures 6*c* and 7). The temperature contours are compressed at the leading edge of the head where the thermal is rising into the cooler ambient fluid, and the axial strain is negative at the forward stagnation (saddle) point.

Figure 8 illustrates the way that fluid elements are advected towards the toroidal vortex defined by the stable manifold of the forward stagnation point. (We use 'vortex' here to describe the spiral geometry of the pathlines, rather than the physical vorticity which is diffused throughout this Stokes flow.) Any region of fluid initially marked by a passive tracer is advected along the pathlines of the effective velocity $\boldsymbol{U} - 2\boldsymbol{\xi}$ and becomes confined near the toroidal vortex. The sequence of shaded regions shown resembles the sequence of shapes – spherical, mushroom, umbrella, toroidal ring – seen in figures 10–12 of Griffiths (1986*b*).

Figure 9 shows vertical profiles of the centreline velocity and temperature for $Ra = 3000$. Head and tail regions are clearly visible in $30 < \zeta < 35$ and $5 < \zeta < 30$

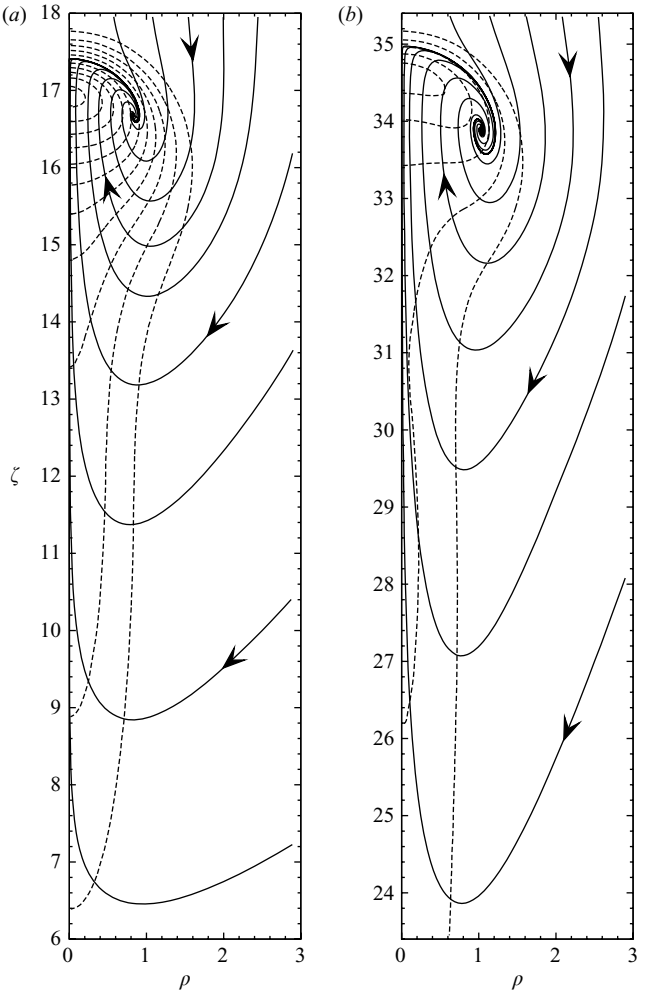

FIGURE 7. Combined pathline (solid) and temperature (dashed) plots for (*a*) $Ra = 1000$ and (*b*) $Ra = 3000$. The pathlines are for the effective advection velocity $\boldsymbol{U} - 2\boldsymbol{\xi}$. The temperature contours are shown at intervals of 8×10^{-3}.

respectively, and the velocity and temperature exhibit a remarkably linear dependence on ζ throughout most of the tail. Similar behaviour is found for all $Ra \gtrsim 1500$. Figure 10 shows several horizontal temperature cross-sections within the tail for $Ra = 3000$. Each cross-section has been rescaled by the centreline value Θ_c, and the data collapse almost perfectly onto the Gaussian form $\Theta(\rho, \zeta) = \Theta_c(\zeta) \exp(-\rho^2/a^2)$, with the width a independent of ζ. This behaviour is also found for $Ra \gtrsim 1500$. Figure 11 shows a global view of the pathlines for $Ra = 3000$, which is typical of the large-Ra behaviour.

For $Ra \gtrsim 1500$, there is a secondary temperature maximum on the axis at the top of the tail, and a weak minimum between this and the start of the head. For $Ra \gtrsim 6000$, the global temperature maximum, which is in the head, moves off the axis to form a horizontal ring (see figure 12). We attribute both of these changes to the cooling effect of colder fluid being advected in under the head, as seen by the pathlines in figures 7 and 12, and by the advection of a patch of passive tracer in figure 8.

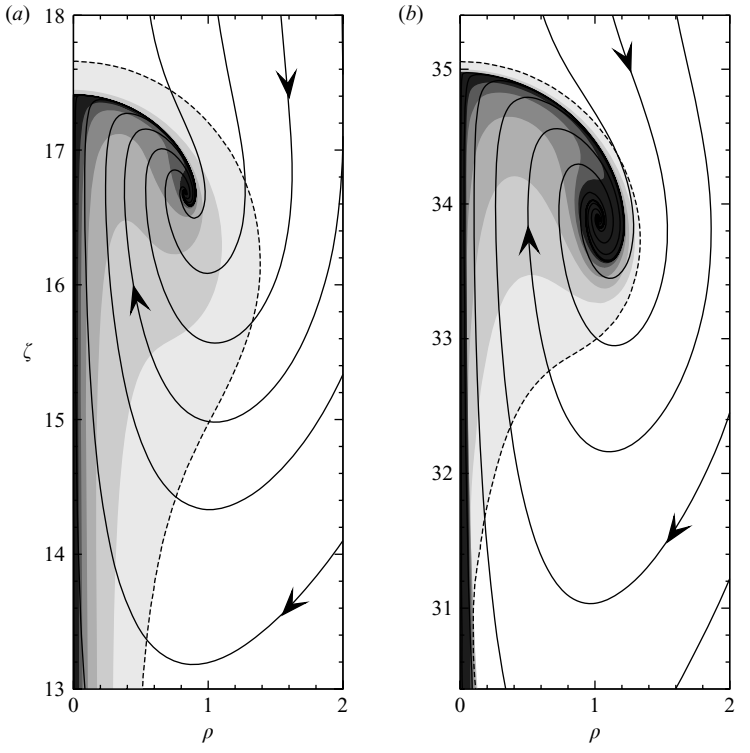

FIGURE 8. The advection of a passive tracer for (*a*) $Ra = 1000$ and (*b*) $Ra = 3000$. The tracer initially occupies the region within the contour $\Theta = 0.016$ (dashed) of the similarity solution (cf. figure 7); the different shaded regions show the region occupied after equal intervals of similarity time τ. The tracer is advected along pathlines (solid) towards the toroidal vortex defined by the stable manifold of the forward stagnation point.

As Ra increases and the tail region lengthens, the global maximum temperature decreases (see figure 13) both in absolute terms and relative to the typical temperatures in the tail. The tail width a decreases only slightly with Ra (see figure 14 below) as does the size of the head region. Since the length and the volume of the tail increase with Ra, the effect of all these changes is that the proportion of the total buoyancy contained in the tail increases with Ra towards 100%, and the proportion in the head decreases to zero.

5. Asymptotic behaviour at large Rayleigh number

We have already seen that as Ra increases, a greater proportion of the buoyancy becomes contained in the tail. In addition, the length scale that dominates the motion in Stokes flows tends to be the largest dimension (in this case the length of the tail), with the smaller width for a slender body contributing only through a logarithmic factor of the aspect ratio. We therefore expect the tail region to be key in understanding the behaviour at large Ra.

In this section, we develop a model for the tail and show that it compares well with our numerical results. In particular, we consider the variation with Ra of the width a and length ℓ of the buoyancy distribution, the gradients Γ and G of the centreline velocity and temperature in the tail, and the mean rise velocity $\overline{W}$.

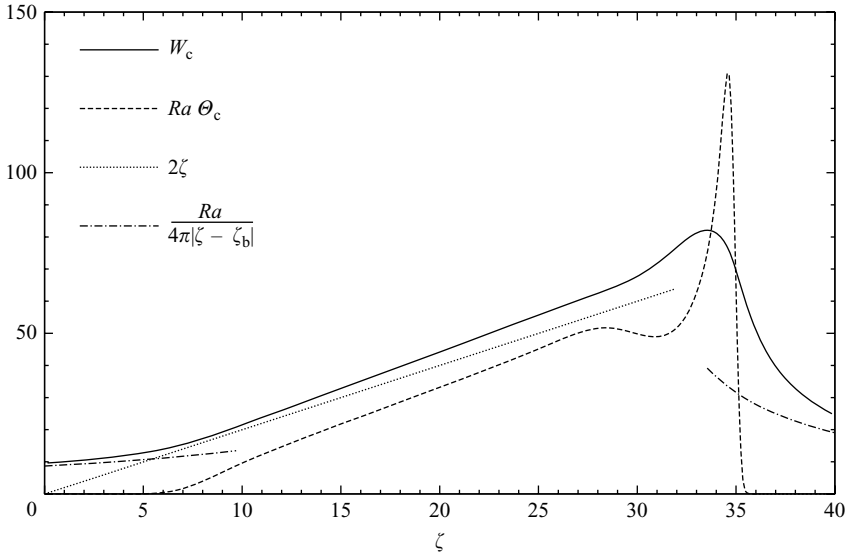

FIGURE 9. Vertical profiles of the centreline temperature Θ_c and vertical velocity W_c for $Ra = 3000$. Also shown is the velocity 2ζ associated with the expanding similarity frame, and the far-field Stokeslet velocity $Ra/(4\pi|\zeta - \zeta_b|)$ (where $\zeta_b \approx 27$ is the height of the centre of buoyancy). Observe the almost perfect linear behaviour of W_c and Θ_c over most of the tail region $5 < \zeta < 30$. Similar results are obtained for other $Ra \gtrsim 1500$.

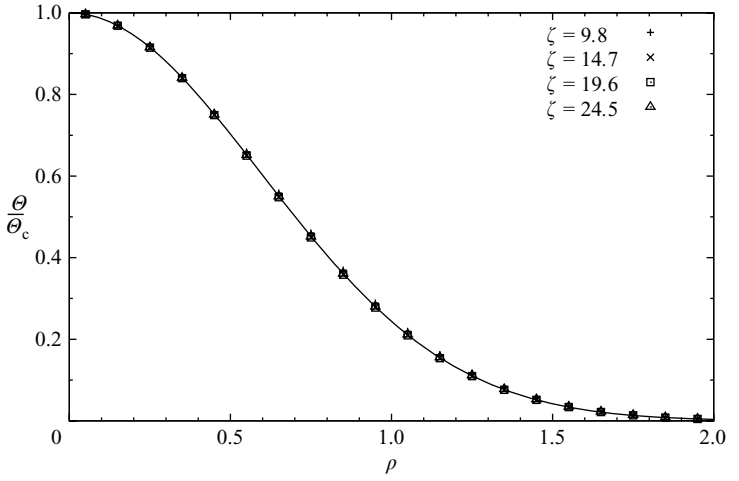

FIGURE 10. Equally spaced horizontal temperature profiles within the tail for $Ra = 3000$. The temperature values in each section have been scaled by the centreline temperature $\Theta_c(\zeta)$. The solid line is $\Theta = \Theta_c \exp(-\rho^2/a^2)$, where $a = 0.842$. Other values of Ra exhibit similar behaviour, and the slight variation in a is shown in figure 14.

5.1. *A simple asymptotic model for the tail*

By integrating the heat equation (2.16) in steady state over a horizontal slice, and noting that $\Theta \to 0$ as $\zeta \to \pm\infty$, we obtain

$$\int_0^\infty \left[\frac{\partial \Theta}{\partial \zeta} + (W - 2\zeta)\Theta\right] 2\pi\rho \, \mathrm{d}\rho = 0. \tag{5.1}$$

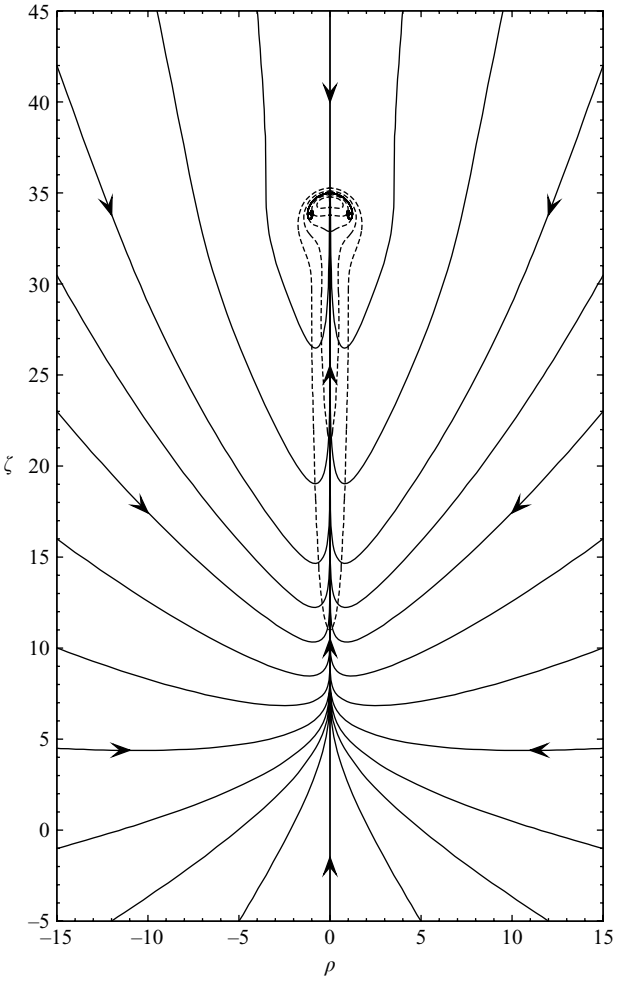

FIGURE 11. Combined pathline (solid) and temperature (dashed) plot for $Ra = 3000$. This is a zoomed-out view of figure 7(a), in order to show the global behaviour of $\boldsymbol{U} - 2\boldsymbol{\xi}$. In the far field, the $-2\boldsymbol{\xi}$ term due to the coordinate expansion dominates and fluid initially moves towards the origin of the similarity frame. Fluid approaching the head from above is deflected around it. Fluid approaching the buoyancy in the tail is deflected upwards and then travels up through the tail and into the toroidal vortex in the head.

In other words, the net vertical heat flux through each horizontal cross-section is zero.

We begin the modelling by assuming that the temperature distribution is vertically elongated, so that the height ℓ is much larger than the width a. Vertical derivatives will then typically be much smaller than their horizontal counterparts. Therefore the vertical diffusion term $\partial\Theta/\partial\zeta$ in (5.1) is negligible compared with the advection terms. Also, there will be little variation in the vertical velocity across the width of the tail. We therefore obtain $W \sim 2\zeta$ as the leading-order balance in (5.1). Applying mass conservation to determine U from W, we obtain the stagnation-point flow

$$(U, W) \sim \left(-\tfrac{1}{2}\Gamma\rho,\ \Gamma\zeta\right), \tag{5.2}$$

where

$$\Gamma \sim 2. \tag{5.3}$$

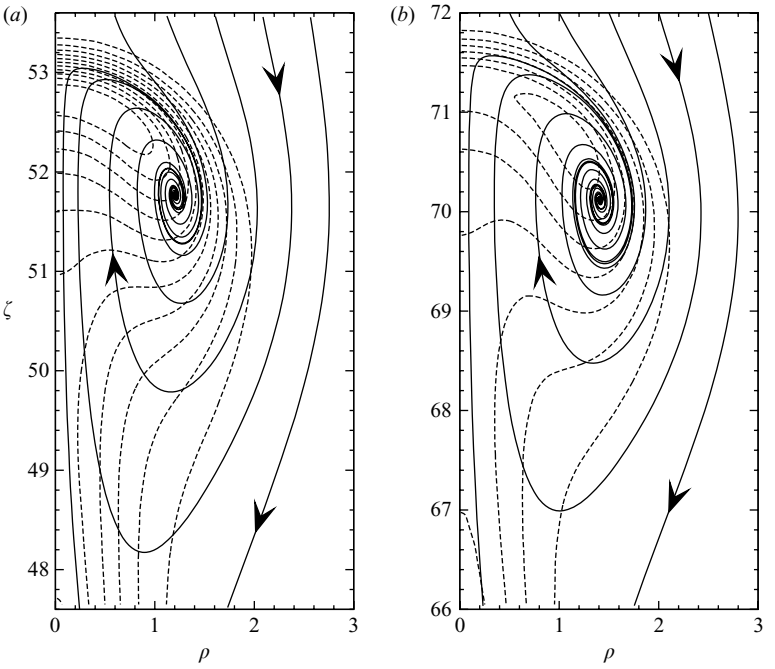

FIGURE 12. Combined pathline (solid) and temperature (dashed) plots as in figure 7. (*a*) $Ra = 6000$, and (*b*) $Ra = 10\,000$. The maximum temperature no longer occurs on the axis.

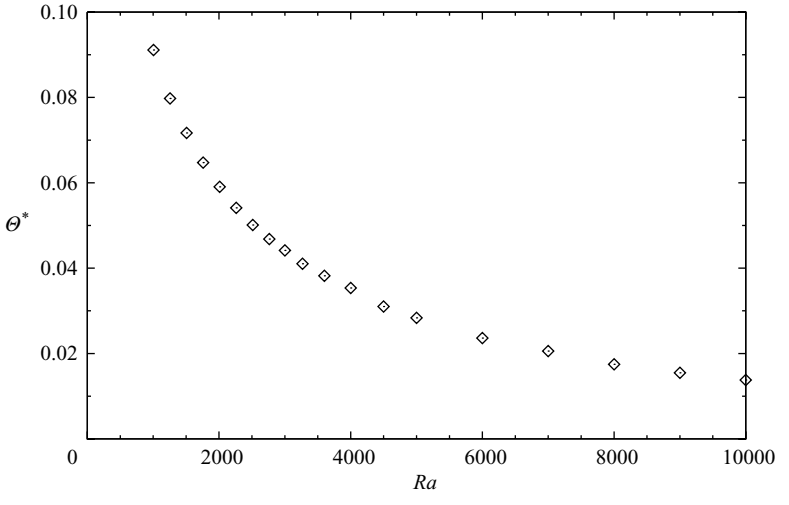

FIGURE 13. Numerical results for the maximum temperature on the axis Θ^* as a function of Ra. For $Ra \gtrsim 6000$ this is slightly smaller than the global maximum temperature, which lies off the axis.

Returning to the full heat equation (2.16), the vertical advection terms cancel at leading order, and vertical diffusion is much smaller than horizontal diffusion. Therefore the leading-order balance is between horizontal advection and horizontal

diffusion. We obtain

$$\frac{1}{\rho}\frac{\partial}{\partial\rho}\left(\rho\frac{\partial\Theta}{\partial\rho}\right)+3\rho\frac{\partial\Theta}{\partial\rho}+6\Theta=0, \tag{5.4}$$

which yields

$$\Theta=g(\zeta)\,\mathrm{e}^{-\rho^2/a^2}, \tag{5.5}$$

where $g(\zeta)$ is an as yet unknown function of ζ, and

$$a^2=\tfrac{2}{3}. \tag{5.6}$$

Applying slender-body theory (see Hinch 1991, § 5.4), we find that the induced vertical velocity W at each height is

$$W\sim\frac{F}{2\pi}\ln\left(\frac{\ell}{a}\right) \tag{5.7}$$

at leading order, where

$$F=Ra\int_0^\infty\Theta\;2\pi\rho\,\mathrm{d}\rho=\pi a^2Ra\,g(\zeta) \tag{5.8}$$

is the horizontally integrated buoyancy at that height. Using (5.2) and (5.8) to eliminate F and W from (5.7), we obtain $g(\zeta)=G\zeta$, where the uniform temperature gradient G is related to Γ by

$$\Gamma\sim\frac{a^2Ra\,G}{2}\ln\left(\frac{\ell}{a}\right). \tag{5.9}$$

The temperature distribution is therefore given by

$$\Theta\sim G\zeta\mathrm{e}^{-\rho^2/a^2} \tag{5.10}$$

for $0<\zeta<\ell$. Application of the buoyancy normalization (2.18) gives

$$\frac{\pi G\ell^2a^2}{2}\sim1, \tag{5.11}$$

and the rise velocity is evaluated from (2.19) as

$$\overline{W}\sim\tfrac{2}{3}\Gamma\ell. \tag{5.12}$$

Combining (5.3), (5.6), (5.9), (5.11) and (5.12), we obtain the following leading-order scalings:

$$a\sim\left(\tfrac{2}{3}\right)^{1/2}, \tag{5.13}$$

$$\ell\sim\left(\frac{Ra\ln Ra}{4\pi}\right)^{1/2}, \tag{5.14}$$

$$\Gamma\sim2, \tag{5.15}$$

$$G\sim\frac{12}{Ra\ln Ra}, \tag{5.16}$$

$$\overline{W}\sim\frac{2}{3}\left(\frac{Ra\ln Ra}{\pi}\right)^{1/2}. \tag{5.17}$$

5.2. *Model comparison*

Some of the predictions of § 5.1 are compared with the numerical results in figures 9, 10 and 14–16. Figure 9 shows that the predicted linear behaviour of the centreline

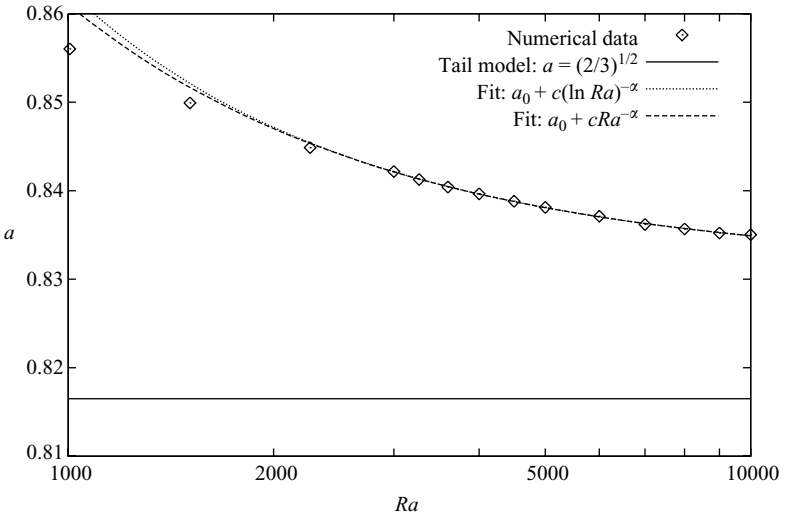

FIGURE 14. The tail width a as a function of Ra. The width is determined by fitting $\Theta_c(\zeta)\exp(-\rho^2/a^2)$ to the numerical results for $\Theta(\rho,\zeta)$ over the linear part of the tail. The data for $Ra > 2500$ are fitted well by either of the forms shown in the legend, with the limiting values a_0 being 0.831 and 0.830, and the exponents α being 0.92 and 6.9, respectively.

velocity and temperature is indeed seen for $Ra = 3000$, though the zero points do not correspond to the coordinate origin (particularly for the temperature). Although not shown, similar behaviour is seen for other values of $Ra \gtrsim 1500$.

Figure 10 shows that the horizontal temperature profiles at $Ra = 3000$ are indeed Gaussian to a good approximation, though the width a is around 0.841 rather than the predicted value of 0.816. Other values of Ra also lead to Gaussian behaviour, and figure 14 shows the variation of the width a with Ra. While there is a slow decreasing trend towards 0.816, the value of a appears to be tending to a finite limit around 0.83.

Figures 15 and 16(a–c) compare the numerical results with the other parameters estimated by the model. The agreement for the mean rise velocity $\overline{W}$ (figure 15) is particularly good, and the velocity gradient Γ (figure 16a) is only underestimated by 10–15%. Some underestimate is to be expected here, since the model assumes that the vertical velocity is horizontally uniform and that there is no downward conduction of heat. The true centreline velocity must therefore be larger than that predicted, since it must provide extra upward advection to account for the lower velocity away from the axis and the effect of downward conduction in the vertical heat balance (5.1).

The agreement for the temperature gradient G (figure 16b) and length ℓ (figure 16c) is less good, being out by a factor of about 2 in each case. However, the overall trends are captured correctly by this simple model, and the discrepancies are largely addressed by extensions to the model as described below.

5.3. *Extended model for the tail*

Two improvements are now made to the model of § 5.1, which lead to better agreement with the numerical results. First, we improve upon the slender-body estimate (5.9) which links the velocity and temperature gradients. Secondly, we take into account the fact that the vertical velocity decreases slightly away from the axis when considering the vertical heat-flux balance in (5.1). As outlined briefly in Appendix C, these

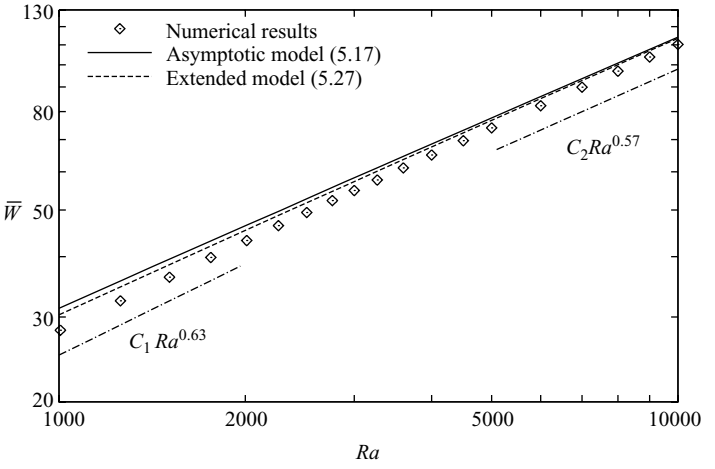

FIGURE 15. The mean rise velocity $\overline{W}$ as a function of Ra. Numerical results and the predictions of the two models are shown. The slope $\mathrm{d}(\ln \overline{W})/\mathrm{d}(\ln Ra)$ varies from about 0.63 to 0.57 across the plot, which is consistent with the $(Ra \ln Ra)^{1/2}$ behaviour of the models in § 5.1 and § 5.3, and clearly different from the $Ra^{3/4}$ proposed by Griffiths (1986*a*; see table 1).

improvements do not include all the corrections required for a formal asymptotic solution at next order, but they do give a much better analytical approximation to the full numerical results. The complete next-order solution can only be computed numerically, and the remaining corrections offer little quantitative improvement.

In the original asymptotic model, slender-body theory allowed us to calculate the leading-order buoyancy field (5.5) from the leading-order velocity (5.2). For simplicity, we assume that a better approximation for the buoyancy field can be found in the form

$$\Theta = \begin{cases} G(\zeta - \zeta_0)\,\mathrm{e}^{-\rho^2/a^2} & \text{for } \zeta_0 < \zeta < \ell + \zeta_0, \\ 0 & \text{otherwise,} \end{cases} \tag{5.18}$$

where the free parameters G and ζ_0 are to be determined, ℓ is given by the buoyancy normalization (5.11), and $a^2 = 2/3$ as before. The form of (5.18) can be partly motivated by the leading-order model and the numerical results. For example, (5.18) is a special case of (5.5) and the vertical offset ζ_0 can be seen in figure 9. In detail, however, it is justified by the analysis outlined in the Appendices.

Given a buoyancy distribution in the form of (5.18), an improved approximation of the induced velocity field can be calculated as described in Appendix B. From (B 8) the centreline velocity gradient Γ is now related to the buoyancy gradient G by

$$\Gamma \sim \frac{a^2 Ra\, G}{2}\left(\ln\left(\frac{\ell}{a}\right) + \frac{\gamma}{2} - \frac{3}{2}\right). \tag{5.19}$$

If we took only the leading-order logarithmic term on the right-hand side, then (5.19) would reduce to (5.9) of the asymptotic model.

Turning to the vertical heat flux condition (5.1), we neglect the $\partial\Theta/\partial\zeta$ contribution as before, and substitute for Θ and the improved estimate of W. We obtain

$$G\tilde{\zeta}\int_0^\infty \mathrm{e}^{-\rho^2/a^2}(Ra\, G\, W_\mathrm{i} - 2\tilde{\zeta} - 2\zeta_0)\, 2\pi\rho\, \mathrm{d}\rho = 0, \tag{5.20}$$

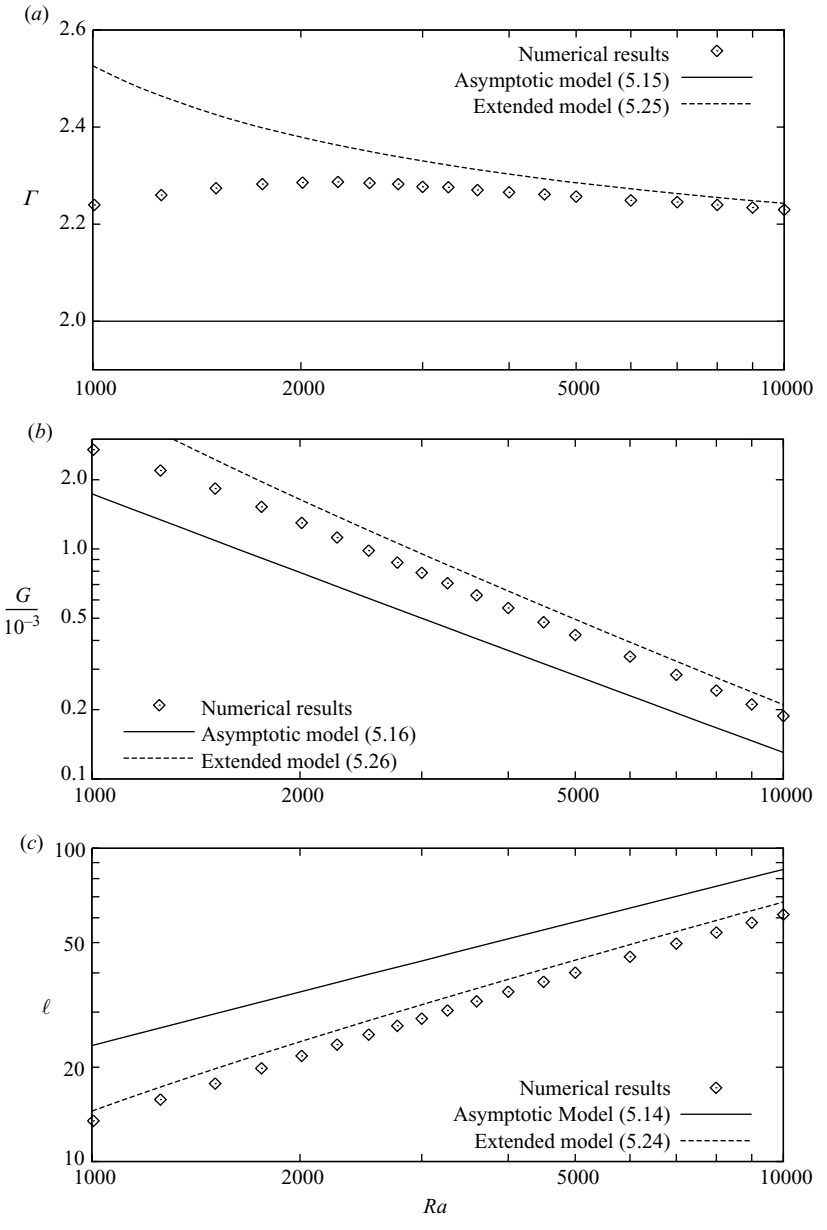

FIGURE 16. Numerical results and some predictions of the two models as functions of Ra. The vertical gradients (*a*) $\Gamma = \mathrm{d}W_c/\mathrm{d}\zeta$ of the centreline velocity and (*b*) $G = \mathrm{d}\Theta_c/\mathrm{d}\zeta$ of the centreline temperature, each in the linear part of the tail. (*c*) The vertical length ℓ of the thermal. (For the numerical results, ℓ is taken to be the distance between the extrapolated zero of the linear centreline temperature in the tail and the position of maximum temperature on the axis.)

where $\tilde{\zeta} = \zeta - \zeta_0$ and $W_i(\rho, \tilde{\zeta})$ is given by (B 6) and (B 8). The integrand in (5.20) is only a linear function of $\tilde{\zeta}$. Consideration of the coefficients of $\tilde{\zeta}^1$ and $\tilde{\zeta}^0$ yields

$$\frac{a^2 Ra\, G}{2}\left(\ln\left(\frac{\ell}{a}\right) + \frac{\gamma}{2} - \frac{3}{2} - \frac{\ln 2}{2}\right) \sim 2 \tag{5.21}$$

and

$$\frac{a^2 \ell Ra\, G}{4} \sim 2\zeta_0, \tag{5.22}$$

which determine G and ζ_0. Comparing (5.19) with (5.21), we see that the centreline velocity gradient Γ is slightly greater than 2, which compensates for the decrease in the vertical velocity away from the centreline. We can also substitute the leading-order term from (5.21) into (5.22) to obtain

$$\zeta_0 \sim \frac{\ell}{\ln(\ell/a)}, \tag{5.23}$$

and show that the offset ζ_0 satisfies $a \ll \zeta_0 \ll \ell$.

The new results (5.19) and (5.21) lead to the revised large-Ra scalings

$$\ell \sim \left(\frac{Ra\, f(C/Ra)}{4\pi}\right)^{1/2}, \tag{5.24}$$

$$\Gamma \sim 2 + \frac{2\ln 2}{f(C/Ra)}, \tag{5.25}$$

$$G \sim \frac{12}{Ra\, f(C/Ra)}, \tag{5.26}$$

$$\overline{W} \sim \frac{2}{3}\left(\frac{Ra\, f(C/Ra)}{\pi}\right)^{1/2}\left(1 + \frac{3}{2f(C/Ra)}\right), \tag{5.27}$$

where $C = 8\pi a^2 e^{3-\gamma} \approx 189$, and $f(x)$ is defined to be the solution of $x = f\exp(-f)$ such that $f(x) > 1$ for $0 < x < e^{-1}$. The large-Ra asymptotic behaviour is still as in (5.13)–(5.17), but numerically significant logarithmic correction terms are also built in. The improvements can be seen in figures 15 and 16, where there is good agreement between the extended model and the numerical results. The remaining corrections at this order, the higher-order corrections in the slender-body expansion in powers of $[\ln(\ell/a)]^{-1}$, and the higher-order correction due the buoyancy in the head all need numerical evaluations. We therefore leave the theoretical development with the good analytical predictions of the extended model.

6. Discussion and conclusions

6.1. *Summary*

We have calculated exact similarity solutions to the full Stokes and temperature equations for the rise of an isolated constant-viscosity thermal in Stokes flow. As Ra increases from zero, the initially spherically symmetric Gaussian temperature distribution of Morton *et al.* (1956) is displaced upwards and becomes deformed, with a wake or tail beginning to form at the rear. At large Ra, the temperature distribution has a roughly spherical head and a long tail stretching back almost to the origin. These changes with Ra can be seen in figures 6, 7 and 12. The largest temperature gradients define the leading edge of the head, which is roughly hemispherical.

The size of the head (based on the width over which the temperature is more than a fixed percentage of its maximum value) varies little with Ra, but the maximum temperature in the head decreases (figure 13) so that the total buoyancy in the head tends to zero as $Ra \to \infty$. At large Ra, most of the buoyancy is thus contained in the tail, which extends most of the way back to the origin (figure 9). Hence, the velocity

	Present results	G86a
a	1	$Ra^{1/4}$
ℓ	$(Ra \ln Ra)^{1/2}$	$Ra^{1/4}$
Θ^*	$(Ra \ln Ra)^{-1/2}$	$Ra^{-3/4}$
$\overline{W}$, ζ_b	$(Ra \ln Ra)^{1/2}$	$Ra^{3/4}$
α	$(Ra \ln Ra)^{-1/2}$	$Ra^{-1/2}$

TABLE 1. Comparison of the asymptotic behaviour of the large-Ra models (either asymptotic or extended) presented here with that of Griffiths (1986*a*). The semi-angle α of the cone swept out by the rising thermal is given by $\tan\alpha \sim a/\zeta_b$. The results of Griffiths (1986*a*) have been converted to the similarity variables used herein, and for simplicity $O(1)$ factors have been omitted. The factors for the present asymptotic model can be seen in (5.13)–(5.17), with the extended results in (5.24)–(5.27).

field is dominated by the buoyancy in the tail. The centreline temperature and vertical velocity are both linear functions of height over most of the tail, and the horizontal temperature profiles there are Gaussian (figures 9 and 10).

The topology of the material trajectories in the similarity frame (given by the effective advection velocity $\boldsymbol{U} - 2\boldsymbol{\xi}$) changes at $Ra \approx 100$. For larger Ra the material trajectories in the head show characteristics of a toroidal vortex and spiral towards an attracting ring at the centre of the vortex (see figure 12). Calculations of the advection of a region of passive tracer (figure 8) give a sequence of shapes – spherical, mushroom, umbrella, toroidal ring – that closely resembles the sequence seen in the advection of a region of dyed fluid in experiments (e.g. figures 10–12 of Griffiths 1986*b*).

In § 5 we developed an asymptotic model for the tail, and an extended model with some of the next-order corrections, which compare well with the numerical results. This agreement strongly supports the idea that the asymptotic dynamics of the rise at large Rayleigh number are controlled by the tail, rather than the head.

6.2. *Comparison with the model of Griffiths (1986a)*

The time-dependences in the scalings for the diffusive growth, cooling and ascent of the thermal (as outlined in § 2.2) are the same as those in the simple geometrical model of Griffiths (1986*a*). The equivalence of the temporal scalings is inevitable on dimensional grounds owing to the form of the equations and to the fact that any length scale derived from the problem parameters must be proportional to $t^{1/2}$. (The only dimensionless groups are Pr and Ra, which are both independent of time.) These temporal scalings are also consistent with the experimental observations in Griffiths (1986*a*).

However, the scalings with Ra obtained here from numerics and the large-Ra asymptotic model do not match those of Griffiths (1986*a*), as can be seen by the comparisons in table 1. (Since the Griffiths model has the same temporal scalings, direct comparisons can be made using our similarity variables.) The different Ra scalings are a consequence of the different buoyancy distributions in the models. The Griffiths model assumes that the buoyancy remains concentrated in a compact and roughly spherical head, which leads to a rise velocity that increases like $Ra^{3/4}$. Our asymptotic model predicts that the buoyancy does not remain in a compact head, and instead most of it is spread over an elongated tail, giving a smaller rise velocity that increases like $(Ra \ln Ra)^{1/2}$. On the one hand, the Griffiths scalings for the dimensions

and rise velocity of the thermal are clearly inconsistent with our numerical results, as seen in figures 14, 15 and 16(*c*). On the other hand, the $Ra^{3/4}$ scaling for the rise velocity (or height), in particular, agrees well with the experimental measurements. This is all somewhat puzzling and merits discussion. We first make a brief mathematical point, and then discuss the experimental evidence in the next section.

Griffiths (1986*a*) comments (p. 136) that a major assumption of his model is that "all the heat in the boundary layer [around the head] is entrained, conserving the total buoyancy of the thermal and preventing the formation of a warm trail". While conceding that there may be some buoyancy loss into a thermal wake, he argues that the loss from the outer edge of a boundary layer would be small, and that the solution with constant buoyancy gives a satisfactory description of the experimental results. The mathematical point is that any heat loss from a compact thermal prevents it from being the long-term solution. As shown by Griffiths (1986*b*), the pathlines in the expanding frame for a compact roughly spherical thermal at large Ra take the form shown schematically in figure 17(*a*). There is a forward stagnation point and an attracting ring within the thermal, and a rear stagnation point just behind the thermal. (Since W falls off rapidly behind the thermal on its radial scale, there is a rearward point where $W = 2\zeta$.) The stable manifold of the rear stagnation point defines a critical surface extending to infinity, which separates pathlines that end near the origin from those that end in the head. Diffusion across this critical surface must result in a net loss of buoyancy from the thermal and these losses, however small, would accumulate over time. Eventually the buoyancy left behind in the thermal wake has a greater dynamical effect than that still in the head, and the flow structure changes to that shown schematically in figure 17(*b*), and seen in our calculated similarity solutions. The elongated buoyancy distribution ensures that $W > 2\zeta$ on the centreline between the head and the origin. There is then no rear stagnation point, all material paths eventually converge into the head, and the buoyancy loss is avoided.

6.3. *Comparison with the experiments of Griffiths (1986a)*

It is not possible to assess from the experimental photographs how much heat loss there is from the head. As noted previously, the dye is, to a good approximation, a passive tracer and thus visualizes the buoyant fluid initially injected from the experimental source rather than any ambient fluid that has been warmed. Our calculations and the Griffiths model both give similar patterns of tracer evolution to those observed. The shadowgraph images (e.g. figure 4*c* of Griffiths 1986*a*) clearly reveal the sharp temperature gradients at the leading edge of the head but do not give a clear picture of what is happening at the rear, where the temperature gradients are much weaker. The $t^{1/2}$ growth of the thermal is common to all models and there is little difference in the predictions of the cone angle α that is swept out (table 1).

The key piece of evidence in support of the Griffiths model is the data on the rise of the top of the thermal. After discarding a short post-release transient, fits of the form $z - z_* = K[\kappa(t - t_*)]^{1/2}$ were made (Griffiths 1986*a*, figure 9), with z_*, t_* and K found for each of 21 experiments. A power-law fit to the 21 slopes gave $K \sim Ra^{0.74 \pm 0.03}$ over the range $250 \leqslant Ra \leqslant 25000$ (see Griffiths 1986*a*, figure 10).

We do not believe that this difference from our solution is due to the presence of boundaries in the experiments: while drag on the sidewalls was estimated to reduce rise velocities by typically about 20 %, it would have a greater effect on large-volume, large-Ra thermals and would thus weaken the dependence of K on Ra not strengthen it. We also do not believe that the difference is due to viscosity variations between the hot injected fluid and the cold ambient fluid, since there was no significant difference

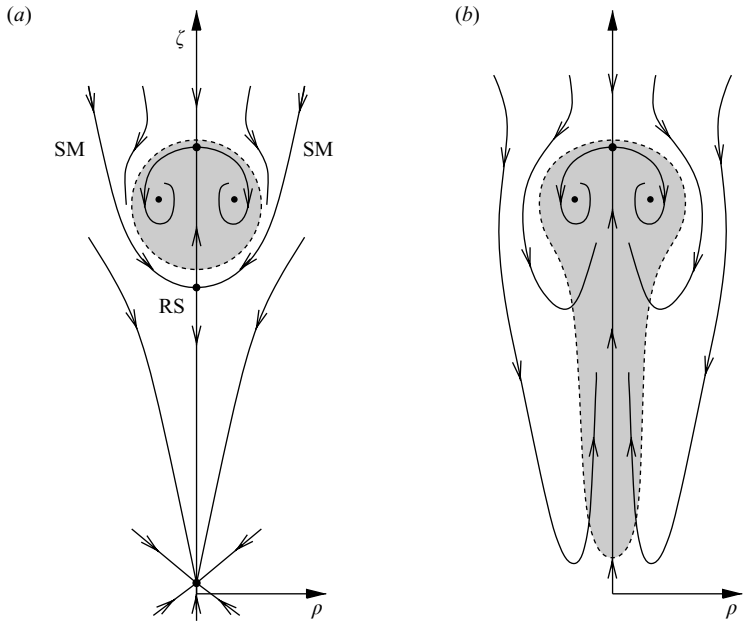

FIGURE 17. Schematic representation of the buoyancy distribution (shaded) and pathlines of $\boldsymbol{U} - 2\boldsymbol{\xi}$ for (a) a compact roughly spherical thermal, as proposed by Griffiths (1986b) and (b) an elongated head-and-tail structure, as revealed by our calculated similarity solutions. In case (a) the buoyancy flux across the stable manifold (SM) of the rear saddle point (RS) prevents it being the long-term solution. For (b) there is no rear stagnation point, and all pathlines eventually reach the head of the thermal.

in the variation of K with Ra between the experiments with injection at 20°C and those with injection at 70°C.

Instead, we note that the duration of the experiments was limited by the finite height of the tank. As a result, the thermals only had room to grow by a factor of 1.5–2.3 (Griffiths 1986a, figure 11), and the duration of the experiment was less, and typically very much less, than the diffusion time $t_D = D_0^2/\kappa$ across the initial diameter D_0 of the thermal. It is plausible that the time taken for arbitrary initial conditions to asymptote onto the exact similarity solution calculated in this paper scales with the diffusion time across the length scale of the initial conditions. By contrast, the post-release transient observed before the Griffiths model gave a good match to the experiments seems comparable to the much shorter advection time $Ra^{-1/2}t_D$ around the thermal. We therefore believe that the experiments were in an intermediate asymptotic regime for which the Griffiths model gives a good transient description. On a longer time scale than the experiments, broadening of the temperature gradients at the edge of the thermal would lead to more and more of the buoyancy leaking away into a thermal wake, until the long-time truly self-similar solution is attained. It is plausible that the initial leakage is slow as Griffiths hypothesized, but would accelerate as the buoyancy and velocity distributions spread from the head to the tail.

6.4. *Other effects and future work*

The preceding discussion motivates a number of problems that might be worth future theoretical examination, both for their own sake and for closer comparison with experiments.

First, it is clearly desirable to have a better understanding of the transient behaviour of a thermal released from some initial condition. In particular the two hypotheses regarding adjustment to the similarity solution on the diffusion time scale seem plausible, but need testing. It would be interesting to know if a thermal with an initial temperature profile that was more Gaussian than top-hat, such as might be produced by a heater or horizontal boundary layer instead of injection, might shed a thermal wake or tail more rapidly. The oscillatory linear eigenmodes seen in the asymptotic decay to self-similarity in § 4 also merit investigation.

Secondly, the presence of boundaries affects the flow, especially given the slow $|\boldsymbol{x}|^{-1}$ decay of the far-field velocity in Stokes flow. The magnitude of boundary effects can be estimated from the method of images by evaluating the velocity field for the unbounded problem at twice the distance to the nearest boundary. Boundaries will have a significant effect when ℓ is comparable to the distance to the nearest boundary and will, in general, disturb the self-similar structure of the solution. An exception to this is the case of a horizontal lower boundary at $z=0$ (since the boundary position is then invariant under the similarity transformation). The method of § 4.1 could easily be adapted to find the similarity solution for this case: a no-flux thermal boundary condition would be applied at $\zeta=0$, and an appropriate image system (see, for example, Pozrikidis 1992, § 3.3) would be added to the velocity Green's function to yield either a stress-free or no-slip condition on the velocity field.

Thirdly, the solution would be affected by variations of the fluid viscosity with temperature. Viscosity variations can be quite large in geophysical situations and with some experimental fluids. The consequent effect on the flow may not be as large as might initially be expected, since the rise of a buoyant blob of one fluid through another is principally governed by the viscosity of the outer fluid rather than the inner. For example, other parameters being equal, the rise of a spherical bubble (zero internal viscosity) is only 25 % faster than that of a spherical drop of equal viscosity to the surrounding fluid (see Batchelor 1967, § 4.9). Therefore, while we would expect a low-viscosity thermal to have a slightly faster rise velocity and a slightly enhanced circulation inside the head, the overall scalings will probably not change by much. The tail-forming tendency may be somewhat reduced as the reasonably warm fluid in the tail rises more rapidly in a Poiseuille-like flow along a 'conduit' formed by the more viscous surrounding fluid (Griffiths & Campbell 1990). The importance of this flow will decrease as the aspect ratio of the thermal increases with Ra. We also note that $T \to T_0$ as the thermal rises and cools, and hence any viscosity contrasts will naturally decay. Therefore at sufficiently large times, the uniform-viscosity solutions presented here will be a good representation of the flow.

Turning the question around, the above considerations also guide the design of experiments intended to give a good comparison with the theoretical solution presented here. The combination of a small heat source and a large tank is clearly necessary to minimize the effects of transients and boundaries. Small temperature contrasts and a fluid, such as silicone oil, with only a weak dependence of viscosity on temperature will minimize viscosity variations. It will be much harder to satisfy all these constraints in a large-Rayleigh-number regime.

Direct applications to the Earth's mantle are fraught with complications as mentioned in the introduction. Since convection from the core–mantle boundary is usually thought to be dominated by plumes rather than thermals, the points of interest may be to address the low temperature excess in plume heads (cf. Farnetani 1997; Bunge 2005) or heat loss during flow past a steady plume (cf. figure 1). Jellinek

& Manga (2004) suggest that convection in other terrestrial planets may be dominated by thermals rather than plumes owing to the absence of plate tectonics.

In conclusion, there is much still to be understood, even in the context of apparently simple theoretical problems that might form building blocks in a more complex picture. Despite the simplifying assumptions used in this work, the exact similarity solution obtained, together with the insights obtained by successful modelling of the large-Rayleigh-number behaviour, form a useful base for further work.

Appendix A. Green's function for an axisymmetric ring of Stokeslets

For the numerical scheme described in § 4.1, we require the Green's function $\boldsymbol{G}$ for the unbounded Stokes flow due to the body force

$$\boldsymbol{f}(\boldsymbol{\xi}) = \delta(\rho - \rho_0)\,\delta(\zeta - \zeta_0)\,\hat{\boldsymbol{e}}_\zeta, \tag{A 1}$$

where (ρ, ϕ, ζ) are cylindrical polar coordinates, and $\hat{\boldsymbol{e}}_\zeta$ is the unit vertical vector. We start from the Stokeslet integral representation

$$\boldsymbol{G}(\boldsymbol{\xi}; \rho_0, \zeta_0) = \int \boldsymbol{J}(\boldsymbol{\xi} - \boldsymbol{\xi}') \cdot \boldsymbol{f}(\boldsymbol{\xi}')\, \mathrm{d}^3\xi', \tag{A 2}$$

where

$$\boldsymbol{J}(\boldsymbol{x}) = \frac{1}{8\pi}\left(\frac{\boldsymbol{I}}{|\boldsymbol{x}|} + \frac{\boldsymbol{x}\boldsymbol{x}}{|\boldsymbol{x}|^3}\right) \tag{A 3}$$

is the Oseen tensor (see Pozrikidis 1992, § 2.2) for unit viscosity. After integrating over the two delta functions, we obtain

$$\boldsymbol{G}(\boldsymbol{\xi}; \rho_0, \zeta_0) = \frac{\rho_0}{4\pi}\int_0^\pi \frac{(\zeta - \zeta_0)(\rho - \rho_0\cos\phi)}{R^3}\hat{\boldsymbol{e}}_\rho + \left(\frac{1}{R} + \frac{(\zeta - \zeta_0)^2}{R^3}\right)\hat{\boldsymbol{e}}_\zeta \,\mathrm{d}\phi, \tag{A 4}$$

where $R^2 = (\zeta - \zeta_0)^2 + \rho^2 + \rho_0^2 - 2\rho\rho_0\cos\phi$. The integral in (A 4) can be written in terms of the complete elliptic integrals, K and E, of the first and second kind. We obtain

$$\begin{aligned}\boldsymbol{G}(\boldsymbol{\xi}; \rho_0, \zeta_0) = {} & \frac{\rho_0(\zeta - \zeta_0)}{4\pi\rho R_+}\left(\mathrm{K}(k) - \frac{(\zeta - \zeta_0)^2 + \rho_0^2 - \rho^2}{R_-^2}\mathrm{E}(k)\right)\hat{\boldsymbol{e}}_\rho \\ & + \frac{\rho_0}{2\pi R_+}\left(\mathrm{K}(k) + \frac{(\zeta - \zeta_0)^2}{R_-^2}\mathrm{E}(k)\right)\hat{\boldsymbol{e}}_\zeta\end{aligned} \tag{A 5}$$

where $R_\pm^2 = (\zeta - \zeta_0)^2 + (\rho \pm \rho_0)^2$ and $k = 2\sqrt{\rho\rho_0}/R_+$. Further details can be found in Pozrikidis (1992, § 2.4). To evaluate the elliptic functions numerically, we followed the method of Lee & Leal (1982).

Appendix B. The Stokes flow driven by an idealized tail

Using matched asymptotics, we consider the Stokes flow with unit viscosity driven by the body force

$$\boldsymbol{f}(\boldsymbol{\xi}) = \begin{cases} (\zeta - \zeta_0)\mathrm{e}^{-\rho^2/a^2}\hat{\boldsymbol{e}}_\zeta & \text{for } 0 < \zeta - \zeta_0 < \ell \\ 0 & \text{otherwise} \end{cases} \tag{B 1}$$

in the limit $a \ll \ell$. We use cylindrical polar coordinates (ρ, ϕ, ζ) to represent the position vector $\boldsymbol{\xi}$.

We first consider the outer flow $\boldsymbol{U}_{\mathrm{o}}$ in $\rho \gg a$, which is driven at leading order by a line of Stokeslets of density $F(\zeta) = \pi a^2(\zeta - \zeta_0)$ for $0 < \zeta - \zeta_0 < \ell$. Using the integral representation (A 2), we write

$$\boldsymbol{U}_{\mathrm{o}}(\boldsymbol{\xi}) = \frac{1}{8\pi} \int_{\zeta_0}^{\zeta_0+\ell} \left(\frac{\hat{\boldsymbol{e}}_\zeta}{|\boldsymbol{\xi} - \zeta' \hat{\boldsymbol{e}}_\zeta|} + \frac{(\boldsymbol{\xi} - \zeta' \hat{\boldsymbol{e}}_\zeta)(\boldsymbol{\xi} - \zeta' \hat{\boldsymbol{e}}_\zeta)}{|\boldsymbol{\xi} - \zeta' \hat{\boldsymbol{e}}_\zeta|^3} \right) F(\zeta') \, \mathrm{d}\zeta'. \tag{B 2}$$

The vertical component of $\boldsymbol{U}_{\mathrm{o}}$ can be rewritten as

$$W_{\mathrm{o}}(\rho, \zeta) = \frac{a^2}{8} \left(2 + \rho \frac{\partial}{\partial \rho} \right) \int_{\zeta_0}^{\zeta_0+\ell} \frac{(\zeta' - \zeta_0) \, \mathrm{d}\zeta'}{\left[(\zeta - \zeta')^2 + \rho^2 \right]^{1/2}}. \tag{B 3}$$

This integral can be evaluated analytically, from which we obtain

$$W_{\mathrm{o}}(\rho, \zeta) \sim \frac{a^2 \tilde{\zeta}}{2} \left\{ -\ln\left(\frac{\rho}{\ell}\right) - \frac{3}{2} + \frac{1}{2} \ln\left(4 \frac{\tilde{\zeta}}{\ell} \left[1 - \frac{\tilde{\zeta}}{\ell} \right] \right) \right\} + \frac{a^2 \ell}{4} + O\left(\frac{\rho}{\ell}\right) \tag{B 4}$$

where $\tilde{\zeta} = \zeta - \zeta_0$, as the asymptotic expression for the inner limit of the outer flow.

Turning to the inner flow $\boldsymbol{U}_{\mathrm{i}}(\rho, \zeta)$ in $\rho = O(a)$, we use boundary-layer approximations to reduce the vertical component of the Stokes equations to

$$\frac{1}{\rho} \frac{\partial}{\partial \rho} \left(\rho \frac{\partial W_{\mathrm{i}}}{\partial \rho} \right) = \tilde{\zeta} \mathrm{e}^{-\rho^2/a^2}, \tag{B 5}$$

for $0 < \tilde{\zeta} < \ell$. Integrating twice, we obtain

$$W_{\mathrm{i}}(\rho, \zeta) = W_{\mathrm{c}}(\zeta) - \frac{a^2 \tilde{\zeta}}{4} (\mathrm{Ei}(\rho^2/a^2) + 2 \ln(\rho/a) + \gamma), \tag{B 6}$$

where $\mathrm{Ei}(x) = \int_1^\infty t^{-1} \mathrm{e}^{-xt} \, \mathrm{d}t$, and $\gamma = 0.5772\ldots$ is Euler's constant. $W_{\mathrm{c}}(\zeta)$ is the centreline velocity, but appears here as an undetermined constant of integration. The outer limit of this inner solution is given by

$$W_{\mathrm{i}}(\rho, \zeta) \sim W_{\mathrm{c}}(\zeta) - \frac{a^2 \tilde{\zeta}}{2} \left(\ln(\rho/\ell) + \ln(\ell/a) + \frac{\gamma}{2} \right). \tag{B 7}$$

Matching the inner and outer solutions (B 4) and (B 7), we obtain an asymptotic expression for the centreline velocity. Neglecting the second logarithmic term in (B 4), which is numerically smaller than $-3/2$ except very close to the ends, we obtain

$$W_{\mathrm{c}}(\zeta) \sim \frac{a^2 \tilde{\zeta}}{2} \left(\ln\left(\frac{\ell}{a}\right) + \frac{\gamma}{2} - \frac{3}{2} \right) + \frac{a^2 \ell}{4}. \tag{B 8}$$

Numerical calculation of the full velocity field (e.g. using the Green's function method described in Appendix A) shows that this expression is indeed a good approximation for $\ell/a \gtrsim 10$. Moreover, for moderate values of ℓ/a, it is significantly better than the leading-order slender-body result, which comprises only the logarithmic term.

Appendix C. Full tail solution at next order

In § 5.3 we described an extended model for the tail at large Ra, building on the leading-order asymptotic model of § 5.1. The Gaussian distribution (5.18) was assumed for simplicity, though it only approximately satisfies the full heat equation (2.16), owing to the small corrections to the uniform strain (5.2) that are revealed by

Appendix B. In order to complete a formal asymptotic correction to the leading-order model, we would write

$$\Theta = \left[G\tilde{\zeta} + g_1(\tilde{\zeta})\right]\mathrm{e}^{-\rho^2/a^2} + \Theta_1(\rho, \tilde{\zeta}) \qquad (0 < \tilde{\zeta} < \ell) \tag{C 1}$$

where g_1 is a small perturbation to the horizontally integrated buoyancy and Θ_1 is a small perturbation from Gaussian form with zero horizontal average, i.e. $\int \Theta_1 \rho \, \mathrm{d}\rho = 0$. From the leading-order solution, $g_1, \Theta_1 \ll G\tilde{\zeta}$.

Following through the calculations of Appendix B yields additional terms proportional to $g_1 \ln(\rho/\ell)$ in (B 4), $g_1 \ln(\rho/a)$ in the outer limit of (B 6) and hence $g_1 \ln(\ell/a)$ in (B 8). The contribution of Θ_1 and the local contribution of g_1 to W_i are both negligible at this order. When we evaluate the heat-flux condition (5.1), we can use g_1 to eliminate the logarithmic term that was previously neglected in (B 4), and thus recover (5.21) and (5.22). Hence

$$g_1(\tilde{\zeta}) = -\frac{G\tilde{\zeta}}{2}\frac{\ln\left[4\tilde{\zeta}(\ell - \tilde{\zeta})/\ell^2\right]}{\ln(\ell/a)}. \tag{C 2}$$

The numerator of this equation is numerically small except very close to $\tilde{\zeta} = \ell$.

The solution for Θ_1 is found by writing $\boldsymbol{U} \sim (-\rho, 2\zeta) + \boldsymbol{U}_1$, where the $O[1/\ln(\ell/a)]$ contribution to $\boldsymbol{U}_1$ can be deduced from Appendix B. Then Θ_1 satisfies (5.4) with the right-hand side replaced by $\boldsymbol{U}_1 \cdot \nabla[G\tilde{\zeta}\exp(-\rho^2/a^2)]$. It is not possible to fully integrate this equation analytically, but numerical solution shows that the contribution of Θ_1 to the next-order correction term for Θ is numerically smaller than the contributions already included in $G\tilde{\zeta}$. Though Θ_1 has zero horizontal average, it makes a numerically small correction to the centreline gradient (5.21), amounting to only about 20 % of that due to the term $(\gamma - 3 - \ln 2)/2$. It does not affect either the velocity field or the vertical heat-flux condition at this order.

In summary, the velocity field $\boldsymbol{U}$ calculated with the extended model in § 5.3 is asymptotically correct at this order, while the buoyancy distribution assumed for simplicity in (5.18) lacks the small corrections shown in (C 1) and (C 2) and is thus not quite linear in $\tilde{\zeta}$.

REFERENCES

Batchelor, G. K. 1967 *An Introduction to Fluid Dynamics*. Cambridge University Press.

Boyet, M. & Carlson, R. W. 2005 ^{142}Nd evidence for early (> 4.53 Ga) global differentiation of the silicate earth. *Science* **309**, 576–581.

Buffett, B. A. 2002 Estimates of heat flow in the deep mantle based on the power requirements for the geodynamo. *Geophys. Res. Lett.* **29**, 7.

Bunge, H.-P. 2005 Low plume excess temperature and high core heat flux inferred from non-adiabatic geotherms in internally heated mantle circulation models. *Phys. Earth Planet. Inter.* **153**, 3–10.

Campbell, I. H. & Griffiths, R. W. 1990 Implications of mantle plume structure for the evolution of flood basalts. *Earth Planet. Sci. Lett.* **99**, 79–93.

Davaille, A., Girard, F. & Le Bars, M. 2002 How to anchor hot spots in a convecting mantle. *Earth Planet. Sci. Lett.* **203**, 621–634.

Davies, G. F. 1999 *Dynamic Earth: Plates, Plumes, and Mantle Convection*. Cambridge University Press.

Farnetani, C. G. 1997 Excess temperature of mantle plumes: The role of chemical stratification across D″. *Geophys. Res. Lett.* **24**, 1583–1586.

Garcimartin, A., Mancini, H. & Perezgarcia, C. 1992 2D dynamics of a drop falling in a miscible fluid. *Europhys. Lett.* **19**, 171–176.

Griffiths, R. W. 1986*a* Thermals in extremely viscous fluids, including the effects of temperature-dependent viscosity. *J. Fluid Mech.* **166**, 115–138.

Griffiths, R. W. 1986*b* Particle motions induced by spherical convective elements in stokes flow. *J. Fluid Mech.* **166**, 139–159.

Griffiths, R. W. 1991 Entrainment and stirring in viscous plumes. *Phys. Fluids* A **3**, 1233.

Griffiths, R. W. & Campbell, I. H. 1990 Stirring and structure in mantle starting plumes. *Earth Planet. Sci. Lett.* **99**, 66–78.

Griffiths, R. W. & Campbell, I. H. 1991 On the dynamics of long-lived plume conduits in the convecting mantle. *Earth Planet. Sci. Lett.* **103**, 214–227.

Hamblin, W. K. & Christiansen, E. H. 1998 *Earth's Dynamic Systems*, 8th edn. Prentice–Hall.

Hinch, E. J. 1991 *Perturbation Methods*. Cambridge University Press.

Jellinek, M. & Manga, M. 2002 The influence of a chemical boundary layer on the fixity, spacing and lifetime of mantle plumes. *Nature* **418**, 760–763.

Jellinek, M. & Manga, M. 2004 Links between long-lived hot spots, mantle plumes, D″, and plate tectonics. *Rev. Geophys.* **42**, RG3002.

Kaminski, E. & Jaupart, C. 2003 Laminar starting plumes in high-Prandtl-number fluids. *J. Fluid Mech.* **478**, 287–298.

Kerr, R. C. & Mériaux, C. 2004 Structure and dynamics of sheared mantle plumes. *Geochem. Geophys. Geosyst.* **5**, Q12009.

Koh, C. J. & Leal, L. G. 1989 The stability of drop shapes for translation at zero Reynolds number through a quiescent fluid. *Phys. Fluids* A **1**, 1309–1313.

Kojima, M., Hinch, E. J. & Acrivos, A. 1984 The formation and expansion of a toroidal drop moving in a viscous fluid. *Phys. Fluids* **27**, 19–32.

Kumagai, I. 2002 On the anatomy of mantle plumes: Effect of the viscosity ratio on entrainment and stirring. *Earth Planet. Sci. Lett.* **198**, 211–224.

Lee, S. H. & Leal, L. G. 1982 The motion of a sphere in the presence of a deformable interface: II. A numerical study of the translation of a sphere normal to an interface. *J. Colloid Interface Sci.* **87**, 81–106.

Loper, D. E. & Stacey, F. D. 1983 The dynamical and thermal structure of deep mantle plumes. *Phys. Earth Planet. Inter.* **33**, 304–317.

Machu, G., Meile, W., Nitsche, L. & Schaflinger, U. 2001 Coalescence, torus formation and breakup of sedimenting drops: Experiments and computer simulations. *J. Fluid Mech.* **447**, 299–336.

Metzger, B., Nicolas, M. & Guazzelli, E. 2007 Falling clouds of particles in viscous fluids. *J. Fluid Mech.* **580**, 283–302.

Morton, B. R. 1960 Weak thermal vortex rings. *J. Fluid Mech.* **9**, 107–118.

Morton, B. R., Taylor, G. & Turner, J. S. 1956 Turbulent gravitational convection from maintined and instantaneous sources. *Proc. R. Soc. Lond.* A **234**, 1–23.

Moses, E., Zocchi, G. & Libchaber, A. 1993 An experimental study of laminar plumes. *J. Fluid Mech.* **251**, 581–601.

Nataf, H.-C. 2000 Seismic imaging of mantle plumes. *Annu. Rev. Earth Planet. Sci.* **28**, 391–417.

Olson, P., Schubert, G. & Anderson, C. 1993 Structure of axisymmetric mantle plumes. *J. Geophys. Res.* **98** (B4), 6829–6844.

Olson, P. & Singer, H. 1985 Creeping plumes. *J. Fluid Mech.* **158**, 511–531.

Pozrikidis, C. 1990 The instability of a moving viscous drop. *J. Fluid Mech.* **210**, 1–21.

Pozrikidis, C. 1992 *Boundary Integral and Singularity Methods for Linearized Viscous Flow*. Cambridge University Press.

Press, W. H., Flannery, B. P., Teukolsky, S. A. & Vetterling, W. T. 1986 *Numerical Recipes: The Art of Scientific Computing*. Cambridge University Press.

Steinberger, B. & O'Connell, R. J. 1998 Advection of plumes in mantle flow: Implications for hotspot motion, mantle viscosity and plume distribution. *Geophys. J. Intl* **132**, 412–434.

Tolstikhin, I. & Hofmann, A. W. 2005 Early crust on top of the Earth's core. *Phys. Earth Planet. Inter.* **148**, 109–130.

Turner, J. S. 1969 Buoyant plumes and thermals. *Annu. Rev. Fluid Mech.* **1**, 29–44.

Whitehead, J. A. & Luther, D. S. 1975 Dynamics of laboratory diapir and plume models. *J. Geophys. Res.* **80** (5), 705–717.

WHITTAKER, R. J. 2007 Theoretical solutions for convective flows in geophysically motivated regimes. PhD Thesis, University of Cambridge. Available online at http://robert.mathmos.net/research/phd/.

WHITTAKER, R. J. & LISTER, J. R. 2006*a* Steady axisymmetric creeping plumes above a planar boundary. Part 1. A point source. *J. Fluid Mech.* **567**, 361–378.

WHITTAKER, R. J. & LISTER, J. R. 2006*b* Steady axisymmetric creeping plumes above a planar boundary. Part 2. A distributed source. *J. Fluid Mech.* **567**, 379–397.